CHEMISTRY OF MATERIALS

pubs.acs.org/cm

Article

Limits to Hole Mobility and Doping in Copper Iodide

Joe Willis,[#] Romain Claes,[#] Qi Zhou, Matteo Giantomassi, Gian-Marco Rignanese, Geoffroy Hautier,* and David O. Scanlon*

Cite This: *Chem. Mater.* 2023, 35, 8995−9006

Read Online

ACCESS | Metrics & More | Article Recommendations | Supporting Information

ABSTRACT: Over one hundred years have passed since the discovery of the p-type transparent conducting material copper iodide, predating the concept of the "electron−hole" itself. Supercentenarian status notwithstanding, little is understood about the charge transport mechanisms in CuI. Herein, a variety of modeling techniques are used to investigate the charge transport properties of CuI, and limitations to the hole mobility over experimentally achievable carrier concentrations are discussed. Poor dielectric response is responsible for extensive scattering from ionized impurities at degenerately doped carrier concentrations, while phonon scattering is found to dominate at lower carrier concentrations. A phonon-limited hole mobility of 162 $cm^2\ V^{-1}\ s^{-1}$ is predicted at room temperature. The simulated charge transport properties for CuI are compared to existing experimental data, and the implications for future device performance are discussed. In addition to charge transport calculations, the defect chemistry of CuI is investigated with hybrid functionals, revealing that reasonably localized holes from the copper vacancy are the predominant source of charge carriers. The chalcogens S and Se are investigated as extrinsic dopants, where it is found that despite relatively low defect formation energies, they are unlikely to act as efficient electron acceptors due to the strong localization of holes and subsequent deep transition levels.

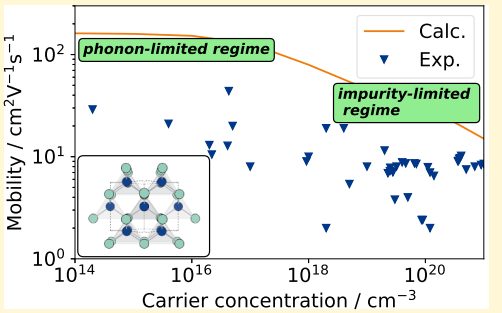

KEYWORDS: *copper, charge transport, holes, mobility, scattering, CuI, defects, density functional theory/DFT*

INTRODUCTION

High mobility p-type transparent conducting materials (TCMs) have eluded researchers for decades. The unlikely bedfellows of good optical transparency (a wide band gap >3 eV and above 90% visible transmission), high valence band dispersion (typically requiring carrier effective mass < $0.5m_e$), and correct point defect chemistry (facile and controllable generation of electron−holes up to 10^{21} cm^{-3}, depending on applications) prove difficult to unite. In fact, these strict requirements preclude the vast majority of materials from ever displaying transparent p-type conducting properties. Early efforts focused on the development of p-type oxides, such as $CuAlO_2$,[1] attempting to mimic the wide optical band gap of the n-type transparent conducting oxides. However, $CuAlO_2$ and other delafossite materials are plagued by low mobility and conductivity due to the polaronic nature of the holes generated in these systems, which are bound to Cu states at the valence band maximum.[2−13]

Several other oxides have been considered as p-type transparent conductors, with varying degrees of success: Li-doped NiO can reach hole concentrations on the order of 1×10^{21} cm^{-3} and conductivity up to 11 S cm^{-1}, but mobility is less than 0.05 $cm^2\ V^{-1}\ s^{-1}$ and transmission drops to 50% upon doping;[14] SnO is a reasonably good p-type TCM, with mobility around 7 $cm^2\ V^{-1}\ s^{-1}$ at 1×10^{17} cm^{-3} carriers, and can also be doped n-type, but incurs stability issues due to the presence of Sn(II) [a problem which pervades ternary Sn(II) materials also];[15,16] quasi-closed shell d^3 and d^6 materials such as Sr-doped $LaCrO_3$ and the ZnM_2O_4 spinels (M = Co, Rh, Ir) have been investigated as TCMs, exploiting the large crystal field splitting between e_g and t_{2g} states to engineer transparency, but their mobilities and conductivities routinely fall short of requirements;[17,18] and Ba_2BiTaO_6, which shows excellent mobility (up to 30 $cm^2\ V^{-1}\ s^{-1}$) due to strong Bi $6s^2$−O 2p interaction at the valence band, but the carrier density is limited to 1×10^{14} cm^{-3}.[19,20] Therefore, research into nonoxides has taken center stage in recent years[21−26] in the hope that greater valence band delocalization and bond covalency can improve hole mobility while simultaneously generating enough carriers to enable degenerate conductivity.

One such material is copper iodide, CuI, first discovered in 1907 by the "father of transparent conductors" Bädeker,[27] and now enjoying somewhat of a renaissance. It crystallizes in the cubic zincblende structure below 643 K (Figure 1a), possesses an optical band gap of around 3 eV, displays native p-type conductivity, and consistently shows one of the highest figures

Received: June 29, 2023
Revised: October 9, 2023
Accepted: October 9, 2023
Published: October 25, 2023

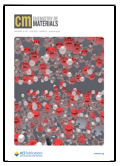

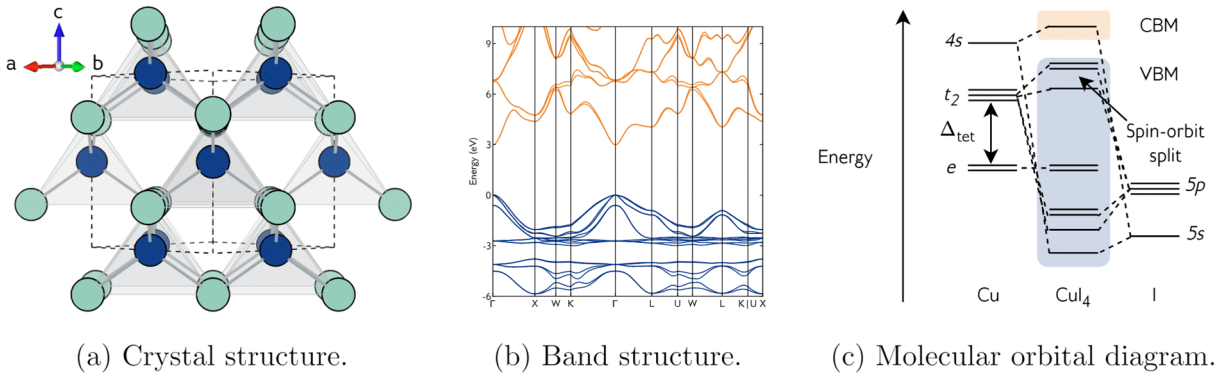

(a) Crystal structure. (b) Band structure. (c) Molecular orbital diagram.

Figure 1. Crystal and electronic structures of CuI. (a) Zincblende crystal structure of CuI, viewed along the face diagonal. Cu and I atoms in blue and green, respectively. Cu atoms have tetrahedral coordination, shown in gray. (b) Electronic band structure of CuI. Calculated using the PBE0 hybrid functional with the inclusion of spin−orbit coupling (SOC). (c) Schematic molecular orbital (MO) diagram of CuI. Upon the inclusion of SOC, further splitting occurs on the t_2—5p MOs into light and heavy hole channels and a spin−orbit split-off band, as seen in (b)

of merit, Φ,[a] for any p-type transparent conductor (over 60,000 $M\Omega^{-1}$ for S-doped CuI).[28−30] It has a disperse, isotropic valence band maximum (Figure 1b), with an average light hole parabolic effective mass of around $0.21m_e$, indicative of a reasonably high hole mobility. The valence band maximum is formed by the interaction of Cu 3d t_2 and I 5p orbitals, while the conduction band minimum is formed by the interaction of Cu 4s with I 5s orbitals,[31,32] as shown schematically in the molecular orbital (MO) diagram in Figure 1c.

$$\Phi = \frac{\sigma}{\alpha} = \frac{-1}{R_s \ln(T_{vis} + R)} \quad (1)$$

where T_{vis} is transmission and R_s is the sheet resistance, related to conductivity and thickness d by

$$R_s = \frac{1}{\sigma d} \quad (2)$$

In addition to its rather attractive electronic structure, the simplicity of CuI is another strong factor in its revival in popularity. Good quality thin films can be deposited via relatively straightforward techniques such as vaporizing iodine onto thin films of copper (à la Bädeker),[33] solid- and solution-based iodization reactions,[34−36] and inkjet printing,[37] while more advanced techniques such as pulsed laser deposition (PLD),[38] molecular beam epitaxy (MBE),[39] and magnetron sputtering are beginning to gain traction.[29] Stability of films in air and to thermal cycling can be improved by encapsulation with amorphous Al_2O_3,[38,40] to prevent the oxidation of Cu(I) to Cu(II). Single crystal growth of CuI is reported more sporadically and over a much narrower range of charge carrier concentrations.[41,42] In terms of devices and applications, CuI has been successfully used in thin film transistors (TFTs) with high operational stability and efficiency,[43] while CuI nanoparticle inks have contributed to improvements in high resolution X-ray imaging technology.[44] This manufacturing simplicity is further enhanced by its strong compatibility with various n-type oxides (such as ZnO, AgI, $BaSnO_3$, and NiI_2), positioning CuI as an optimal contender for combined n- and p-type applications.[45−51]

Despite this fashionable return to the forefront of p-type TCM research, the charge transport behavior of CuI is poorly understood. Experimental reports show no clear trend between hole mobility and carrier concentration, while little computational work has been undertaken on this subject. In this work, the intrinsic limits of CuI as a high-mobility transparent conductor are investigated from first-principles calculations and state-of-the-art charge carrier transport modeling. The intrinsic defect chemistry and the effects of chalcogen doping are examined to estimate the window of achievable charge carrier concentrations in CuI. The different contributions to the overall scattering rate are analyzed using two separate approaches, where it is found that scattering from phonons and ionized impurities dominate at either end of the charge carrier concentration range, respectively.

COMPUTATIONAL METHODOLOGY

Electronic band structure, AMSET inputs, and defect calculations were performed within VASP, a periodic plane-wave code that uses the projector-augmented wave (PAW) method for describing the interaction between core and valence electrons.[52−58] The explicit electron configurations of the pseudopotentials used were as follows: Cu $3d^{10}4s^1$; I $5s^25p^5$; S $3s^23p^4$; and Se $4s^24p^4$. A plane-wave cutoff of 500 eV and a Γ-centered **k**-point mesh of 7 × 7 × 7 were found to converge the total energy to within 1 meV $atom^{-1}$. Structural relaxations were carried out with a plane-wave cutoff of 650 eV to avoid Pulay stress and with a convergence criteria of 0.1 meV $atom^{-1}$. The GGA PBEsol functional was used for all convergence testing and density functional perturbation theory (DFPT)-related inputs,[59] while the hybrid PBE0 functional was used for electronic structure, defect, and finite differences (FD) calculations.[60] For all electronic structure calculations, spin−orbit coupling (SOC) effects were explicitly considered due to the presence of heavy I atoms. Considering the size of the spin−orbit split-off in the electronic band structure, the addition of SOC effects via a single-shot electronic structure calculation after structural optimization is crucial to get the correct value of the band gap and relative band edge positions during defect calculations. SOC effects are negligible when computing structural properties, so they were not included during relaxations.

Charge transport properties were calculated by using both ABINIT and the AMSET package. ABINIT uses a fully first-principles approach to calculate phonon-limited mobilities based on an iterative solver to the Boltzmann transport equation (IBTE).[61−64] The approach used in ABINIT, which is detailed in refs 64 and 65, allow us to achieve a level of performance that is competitive with Wannier-based packages while bypassing the need for Wannier functions altogether.

https://doi.org/10.1021/acs.chemmater.3c01628
Chem. Mater. 2023, 35, 8995−9006

First, our approach takes advantage of the tetrahedron integration scheme to significantly reduce the number of e−ph matrix elements that need to be computed. In addition, we employ a Fourier interpolation of the scattering potentials in **q** space, which includes the accurate treatment of dipole and quadrupole contributions and the exact Kohn−Sham (KS) wave functions are computed only for the **k**-points lying inside a small energy window around the band edges. Here, a convergence is assumed to be reached when three consecutive grids lead to mobilities a maximum 5% away from each other. In CuI, the converged IBTE mobilities were obtained with **k**-meshes of 162 × 162 × 162 and interpolated DFPT scattering potentials and interatomic force constants obtained on a 9 × 9 × 9 coarse **q**-mesh. All the calculations needed to obtain the mobility within ABINIT were done with the GGA PBEsol functional including SOC. The dynamical quadrupoles (Q^*) were also included for the scattering potentials and mobilities. However, as the DFPT computation of Q^* is still limited to norm-conserving pseudopotentials without nonlinear core corrections (NLCC) and without SOC, a slight deviation of the mobility can be expected but by several orders of magnitude less than doing the calculations without taking the Q^* into account.

On the other hand, AMSET solves the linearized Boltzmann transport equation using the relaxation time approximation (RTA). Individual scattering rates were explicitly calculated using material properties, going beyond the constant relaxation time approximation to give a more accurate description of carrier lifetimes. In this study, scattering from polar optical phonons (POP), acoustic deformation potentials (ADP), ionized impurities (IMP), and piezoelectric effects (PIE) were considered, which require deformation potentials, the elastic constant, low- and high-frequency dielectric constants, the polar optical phonon frequency, and the piezoelectric constant. Explicit values (and convergence of these parameters) can be found in the Supporting Information. A dense uniform Γ-centered **k**-point mesh of 14 × 14 × 14 was used to obtain the wave function overlaps for determining scattering rates, and the corresponding band structure was plotted using the SUMO package.[66] The deformation potentials were calculated from density of states calculations using the same convergence parameters as bulk calculations. The low-frequency dielectric constant, piezoelectric constant, and polar optical phonon frequency were calculated using both DFPT and FD implementations in VASP. The high-frequency dielectric constant was calculated with the PBE0 functional using the independent particle random phase approximation (IP-RPA) optics routine in VASP and converged against the number of empty bands and **k**-point density.

Phonon calculations on CuI were performed with DFPT and ABINIT using PBEsol + SOC and a 9 × 9 × 9 **q**-mesh following the methodology used by Petretto et al.[67] The structures were relaxed until all the forces on the atoms and the stresses were below 10^{-6} Ha/bohr and 10^{-4} Ha/bohr^3, respectively, using a plane-wave cutoff of 46 Ha.

Defect calculations were performed with VASP on a 64 atom supercell and with a Γ-centered 2 × 2 × 2 **k**-point mesh. Each defect was fully relaxed using the PBE0 functional, followed by a spin−orbit coupling single-shot calculation to obtain accurate energies. This goes beyond the GGA relaxation plus hybrid single-shot calculations of Graužinytė et al., fully capturing structural distortions caused by charge localization that would otherwise be missed with a semilocal exchange−correlation functional.[68] The potential energy surface was explored using the ShakeNBreak method.[69,70] Defect formation energies were obtained in the usual fashion, within the Lany−Zunger formalism[71−74]

$$\Delta E_f^{(D,q)} = (E^{(D,q)} - E^H) + \sum_i n_i(E_i + \mu_i) + q(\Delta E_F + \epsilon_{VBM}) + \underbrace{\Delta E_{ic}^{LZ\text{-}MH} + \Delta E_{pa}^{LZ} + \Delta E_{bf}^{LZ}}_{\text{post-processing corrections}} \quad (3)$$

The transition level diagrams and self-consistent Fermi level were calculated using the PY-SC-FERMI package.[75,76]

The EFFMASS package was used to analyze the transport effective mass.[77,78]

RESULTS

Crystal and Electronic Structure. The structural properties (lattice parameter, lattice angle, and Cu−I bond length) of CuI are summarized in Table 1, where good agreement is found between the calculated values and both the experimental and computational literature. The PBEsol lattice parameters are slightly underestimated compared to room temperature neutron powder diffraction measurements by Keen and Hull,[79] while the PBE0 results show closer agreement. Low-temperature diffraction data are scarcely reported but are expected to yield lattice parameters closer to the PBEsol results. Thin film CuI often displays slightly larger lattice parameters (6.06 Å from Moditswe et al.)[80] owing to tensile strain between the film and substrate.

Table 1. Structural and Band Structure Properties of CuI

parameter	Exp[79]	PBE0	PBE0 lit[32]	PBEsol
a/Å	6.05	6.08	6.07	5.95
α/°	90.0	90.0	90.0	90.0
Cu−I/Å	2.57	2.63	2.62	2.58
band gap/eV	2.95[81]	2.99	2.97	0.95
SOC splitting energy/eV	0.64[82]	0.63		0.47
hole conductivity effective mass/m_0		0.61		0.72

As shown in Table 1, a direct band gap of 2.99 eV at Γ is calculated with the PBE0 functional including spin−orbit coupling effects (PBE0 + SOC, Figure 1b), which is in good agreement with experimental values obtained from a variety of measurements: pressure-dependent optical absorption from Ves et al., 2.95 eV;[81] transmission spectra from Storm et al., 3.11 eV.[38] This also matches well previous hybrid DFT calculations, with Yu et al. most recently reporting a value of 2.97 eV.[32] On the other hand, the direct band gap computed with PBEsol is severely underestimated, as is often the case in semilocal DFT. The hole conductivity effective mass (or the transport mass) determined from PBE0 calculations is slightly lower than that from PBEsol. Semilocal DFT functionals often struggle to accurately describe localized d states (regardless of electronic occupation) without the inclusion of the Hubbard U parameter, so a mismatch in the transport effective mass is not unexpected.

In CuI, the inclusion of SOC has a direct effect on the band edges. Figure 2a illustrates that without SOC, the valence band maximum (VBM) of CuI has three degenerate bands. The

https://doi.org/10.1021/acs.chemmater.3c01628
Chem. Mater. 2023, 35, 8995−9006

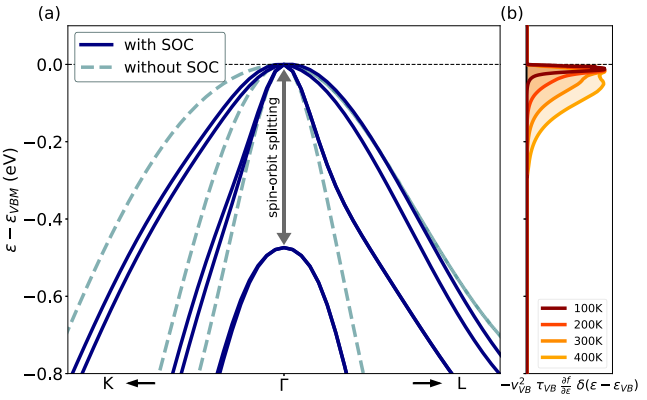

Figure 2. (a) Top of the valence bands of CuI around Γ with and without SOC as computed with the PBEsol functional. (b) The normalized function $-v_{VB}^2 \tau_{VB} \frac{\partial f}{\partial \varepsilon}$, convoluted with $\delta(\varepsilon - \varepsilon_{VB})$ in the valence band at different T. In this expression, v_{VB} and τ_{VB} stand for the carrier velocity and lifetime in the valence band (VB), $\frac{\partial f}{\partial \varepsilon}$ is the derivative of the Fermi−Dirac distribution function with respect to the energy and δ the Dirac delta function. By integration of this function, relaxation time approximation (RTA) hole mobility is obtained.

addition of SOC results in the lifting of the degeneracy, with one of the bands (the split-off band) dropping in energy, a common feature of zincblende semiconductors. As for the band gap, PBEsol tends to undervalue the spin−orbit splitting at the Γ-point of the VBM which is around 470 meV, whereas the value computed with PBE0 is around 630 meV, in excellent agreement with the value of 640 meV determined experimentally by Blacha et al. using hydrostatic pressure-dependent thin-film absorption.[82]

Charge Transport. Two methods are used to simulate charge transport in CuI: an iterative Boltzmann transport equation (IBTE) solution to calculate phonon-limited mobilities using the ABINIT code;[61−64] and a phenomenological model (AMSET) that calculates scattering rates for ADP, PIE, IMP, and POP scattering, utilizing low-cost inputs from first-principles calculations using the VASP code.[52,53,55−58,83] While IBTE provides a high-quality representation of transport properties, AMSET complements the analysis by evaluating the effects of impurities and also by providing an additional analysis of the phonon scattering mechanisms by decoupling the different contributions. AMSET also offers the advantage of using hybrid functionals, which are difficult to employ in fully first-principles IBTE calculations due to the computational cost and absence of implementations able to compute electron−phonon (e−ph) quantities within DFPT. The methodology for each approach is outlined in the Supporting Information.

Iterative Boltzmann Transport Equation. The lifting of degeneracy resulting from the addition of SOC has a clear impact on the hole transport. Indeed, for transport in semiconductors, only energies near the top of the VBM are relevant.[78] As depicted in Figure 2b, the function $-v_{VB}^2 \tau_{VB} \frac{\partial f}{\partial \varepsilon} \delta(\varepsilon - \varepsilon_{VB})$, which once integrated provides direct access to the RTA hole mobility, quickly approaches zero for energies further from the Fermi level. This means that only the electronic states covered by this function participate in hole transport. As a result, the inclusion of SOC in CuI leads to the complete removal of a scattering channel as the split-off band is no longer included in the energy windows responsible for transport, even at higher temperatures. Using ABINIT, we obtain a converged IBTE mobility of 162 $cm^2 V^{-1} s^{-1}$ at 300 K with SOC and dynamical quadrupoles (Q^*) using 162 × 162 × 162 **k**- and **q**-point grids (refer to Figure S2). The inclusion of the SOC leads to an enhancement in mobility by removing a scattering channel. Note that, despite the increase in mobility due to the effect of SOC on the electronic bands, its effect on phonons remains negligible on both phonon band structure and mobility, as shown in Figures S1 and S2. The integration of Q^*, the next order of correction to dynamical dipoles, in the computation is also necessary to obtain accurate results,[63,64] preventing an error of about 15% in the case of CuI.

The DFPT phonon dispersion of CuI is shown in Figure 3a and shows good agreement with the experimental frequencies reported in the literature.[84,85] The minor disparity, such as for the LO-TO splitting, may be attributed to the challenge of precisely capturing the dielectric constants in CuI, as discussed in the next section. This plot is accompanied by the corresponding spectral decomposition of the hole scattering rates at different T (Figure 3b), and shows that the high-frequency longitudinal optical mode T_2 (LO) is the main

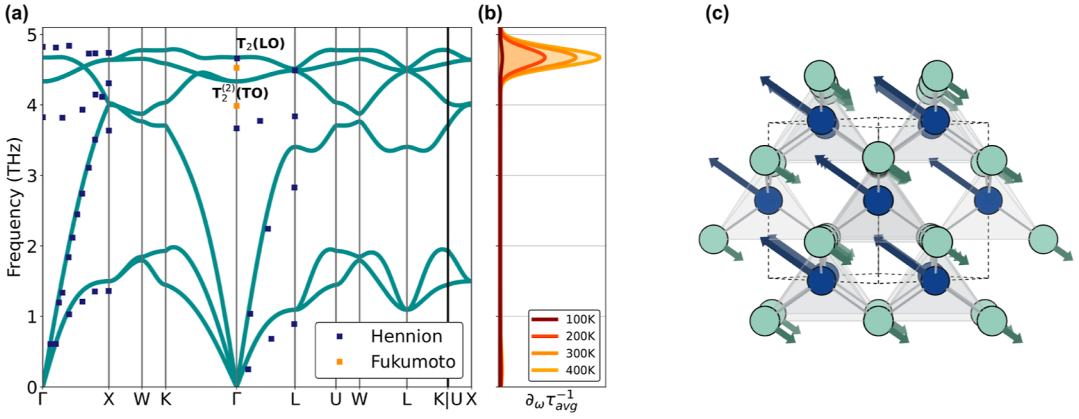

Figure 3. (a) CuI phonon dispersion computed with SOC and the PBEsol functional with experimentally reported frequencies overlaid.[84,85] (b) Spectral decomposition of the hole scattering rates as a function of frequency at different temperatures. (c) Structure of CuI showing the atomic displacements corresponding to the longitudinal optical phonon mode at the Γ point (toward the X direction), viewed along the face diagonal; Cu and I atoms in blue and green, respectively.

https://doi.org/10.1021/acs.chemmater.3c01628
Chem. Mater. 2023, 35, 8995−9006

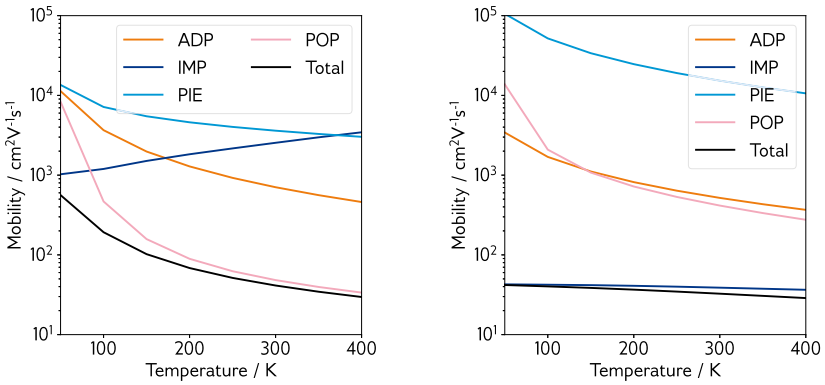

(a) Low carrier concentration, 1×10^{16} cm^{-3}. (b) High carrier concentration, 1×10^{20} cm^{-3}.

Figure 4. CuI hole mobility as a function of the temperature at two carrier concentrations. Colored lines represent mobility contributions from each type of scattering: ADP is acoustic deformation potential scattering (orange); IMP is ionized impurity scattering (dark blue); PIE is piezoelectric scattering (light blue); POP is polar optical phonon scattering (pink); and total is the reciprocal sum of these contributions (black). (a) Low carrier concentration, 1×10^{16} cm^{-3}. (b) High carrier concentration, 1×10^{20} cm^{-3}.

contributor to the e−ph scattering in CuI. Although the spectral decomposition encompasses both short- and long-range phonons, transport in CuI is mainly influenced by the latter ones (near Γ). This is due to the unique and curvy pocket present at the VBM of the electronic band structure of the material, allowing only transitions with a small momentum transfer **q**. Figure 3c represents the T_2 (LO) phonon mode of CuI at Γ (toward the *X* direction) with the Cu and I atoms moving in phase opposition with twice the displacement amplitude for Cu. The relative contribution to scattering increases with *T* due to the growing number of phonons that are thermally excited, as evidenced by the area under the curve of Figure 3b expanding from 100 to 400 K. This results in a decrease of the e−ph IBTE mobility with temperature, as shown in Figure S3.

AMSET. Figure 4 shows the hole mobility calculated with AMSET at low and high carrier concentrations. The mobility is split by scattering mechanism, and the total mobility is plotted as the reciprocal sum of each component (via Matthiessen's rule). At a carrier concentration of 1×10^{16} cm^{-3} (Figure 4a), scattering from POP is predicted to dominate the hole mobility, yielding a total room temperature hole mobility of 41.3 cm^2 V^{-1} s^{-1}. Scattering from ADP, PIE, and IMP is essentially negligible at low concentrations compared to POP scattering. The piezoelectric constant calculated from DFPT is in excellent agreement with the experiment (0.10 C m^{-2} against 0.13 C m^{-2})[86] and confirms that PIE scattering does not compromise the mobility despite the noncentrosymmetric inversion native to the zincblende crystal structure.

Moving to a higher carrier concentration of 1×10^{20} cm^{-3} (Figure 4b), the effects of both POP and PIE scattering are diminished further, while ionized impurities begin to control the charge transport behavior in CuI—a room-temperature hole mobility of 32.6 cm^2 V^{-1} s^{-1} is predicted. IMP (and indeed POP scattering in the AMSET implementation) scattering is largely determined by the value of the static dielectric response of a material, i.e., its ability to screen electric charge. For CuI, calculated dielectric constants range from 5.27 to 8.85, dependent on the flavor of DFT functional and the method used to calculate the high- and low-frequency responses, and are shown in Table 2. Meanwhile, an experimental dielectric response of 6.5 is reported by Hanson et al.[86] Accurate calculation of the dielectric response in tetrahedral semiconductors is benchmarked by Skelton et al.,[87] who note that semilocal DFT nearly always overestimates the high-frequency dielectric response, while hybrid functionals nearly always underestimate the high-frequency dielectric response, with PBE0 performing worse than HSE06. Considering the tetrahedral zincblende structure of CuI, it is reasonable to assume that similar trends are followed here. Due to the fact that the dielectric constant is quite small for CuI, these quite large percentage errors in ϵ_0 have significant effects on the POP and IMP scattering rates, as shown in Figure S4 in the Supporting Information. To this end, the dielectric constant used in the AMSET calculations in Figures 4 and 5 is that determined from experiment (6.5, where ϵ_{ionic} is set as the calculated value of 1.1 from DFPT, and the remainder is assigned to ϵ_∞), with lower and upper limits (5.27 and 8.85) shown for context in the Supporting Information. More sophisticated methods for calculating the dielectric response that can accurately model excited state features, such as *GW* (Green's function *G* with screened Coulomb interaction *W*) and BSE (Bethe−Salpeter equation) implementations, would provide a clearer picture,[88] but exceed the scope of the current work.

Table 2. Dielectric Constants Calculated Using a Variety of Methods[a]

details	ϵ_{ionic}	ϵ_∞	ϵ_0
PBEsol DFPT; PBEsol IP-RPA*	1.10	7.75	8.85
PBEsol DFPT; PBE0 IP-RPA*	1.10	4.17	5.27
PBE0 FD; PBE0 IP-RPA*	1.65	4.17	5.82
materials project: PBE	0.87	6.82	7.69
Li et al.[89] PBE	1.53	4.77	6.30
Hanson et al. (exp.)[86]			6.5

[a]* denotes calculations from this work; DFPT (density functional perturbation theory) or FD (finite differences method) calculations were used to determine the low-frequency, ϵ_{ionic}, response, while IP-RPA (independent particle random phase approximation) optical calculations were used to determine the high-frequency, ϵ_∞, response. Further details can be found in the methodology section.

Combined Approach. While AMSET correctly predicts the relative importance of the different scattering mechanisms, the low concentration regime phonon-limited mobility predicted by AMSET and the IBTE method varies by a factor of 4. As

https://doi.org/10.1021/acs.chemmater.3c01628
Chem. Mater. 2023, 35, 8995−9006

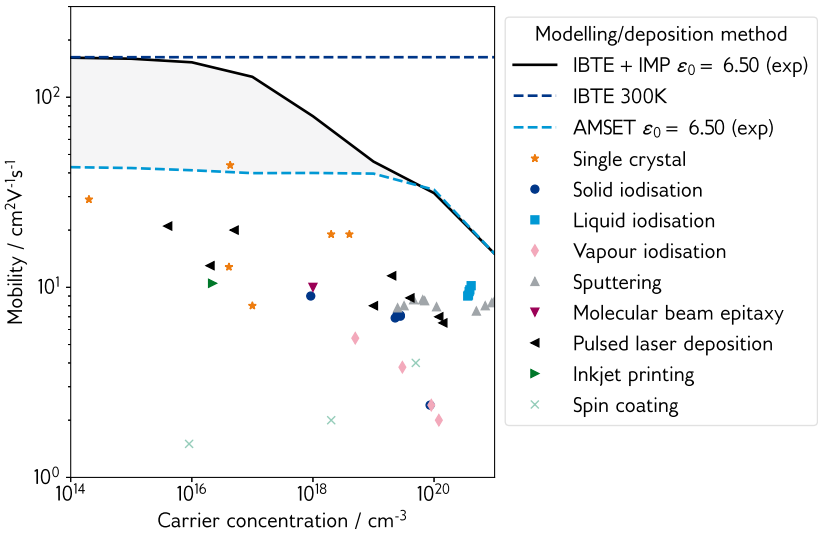

Figure 5. Experimental hole mobility as a function of carrier concentration, broken down by the deposition method. Experimental data are reported in refs 29, 30, 33−35, 37−42, 95−969798. IBTE and AMSET drift mobilities overlaid as dashed lines; IBTE + IMP mobility $\left(\frac{1}{\mu_{\mathrm{IBTE+IMP}}} = \frac{1}{\mu_{\mathrm{IBTE}}} + \frac{1}{\mu_{\mathrm{IMP}}}\right)$ overlaid as a filled black line; gray shaded region denotes space between AMSET-estimated upper limit and IBTE + IMP-estimated upper limit.

POP scattering is the primary mobility-limiting mechanism in this material at low carrier concentrations, this overestimation of the scattering rate results in mobility values that are lower than those reported in the experimental literature (notably the single crystal result from Chen et al.).[41] One way to explain this is the inelastic treatment of POP in AMSET. Indeed, AMSET approximates POP scattering using the self-energy relaxation time approximation (SERTA), which as part of its formalism considers scattering only in the forward direction relative to charge carrier motion. The omission of backward scattering can lead to an underestimation of phonon-limited mobility, the extent of which varies between materials depending on the complexity of the band edge (single band or multidegenerate), the effective mass, and spin−orbit effects.[65,90]

The comparison between phonon-limited mobility and experimental results can be challenging since most calculations do not consider impurities or defects. While SERTA serves as an approximation of IBTE, it is advisible to prioritize the latter due to its comprehensive nature, even if certain SERTA results appear closer to experimental data. For instance in Si, the computed electron mobility with the two methods fall within the range of experimentally reported mobilities,[64] although the hole mobility is overestimated by both approaches—only when performing simulations using the experimental lattice parameter and fitting the band structure to the experimental hole effective mass is agreement with experimental mobility recovered using the IBTE approach;[90] for SiC the IBTE performs better than the SERTA for electron mobility (SERTA underestimates by around 30%), while they straddle the upper and lower side of experimental results for the hole mobility, respectively;[91] and for GaAs both the implementations provide rather unreliable results, not helped by the large range of experimental mobilities reported.[92] Surveying over 50 materials, Claes et al. show that differences in computed mobility using IBTE and SERTA can reach up to 60%,[65] and that the differences are often particularly large for binary halides with low ω_{POP} such as NaI, CsI, and TlBr. The general trend is that SERTA will, if at all, underestimate phonon-limited mobilities compared with the exact IBTE results. Crucially, it is difficult to predict a priori the severity of the underestimation.

To this end, mobility values obtained using SERTA under ABINIT are compared with those acquired using AMSET, as illustrated in Figure S3. It is found that the agreement between the two SERTA results is close, and this indicates that POP scattering is potentially overestimated in AMSET for CuI due to the SERTA. Therefore, we propose that the mobility limit in CuI is determined in the low concentration regime by IBTE e−ph scattering and in the high concentration regime by ionized impurity scattering.

Figure 5 shows the hole mobility determined by summing the e−ph contribution from IBTE and the IMP contribution from AMSET assuming the validity of Matthiessen's rule on mobility $\left(\frac{1}{\mu_{\mathrm{IBTE+IMP}}} = \frac{1}{\mu_{\mathrm{IBTE}}} + \frac{1}{\mu_{\mathrm{IMP}}}\right)$. While this does not represent an exact solution to the BTE, it provides a reasonable upper limit to the mobility that is achievable in CuI. The e−ph IBTE and total AMSET drift mobilities (computed using the experimentally determined dielectric constant of 6.5) are also shown, as are experimental Hall mobility values from the literature. As the Hall factor (r_{H}) is close to 1 for CuI and CuBr,[93,94] it is reasonable to compare the simulated drift mobility with experimental Hall mobility ($r_{\mathrm{H}}\mu \sim \mu_{\mathrm{H}}$).

The combined mobility from IBTE and IMP acts as an upper limit to hole mobility in CuI, within which the presently available data from experiment falls. First, single crystal data are considered (orange stars in Figure 5), which should represent the highest achievable experimental mobility and truest comparison to simulation, as only the intrinsic, material-dependent scattering processes should be present. It is well-known however that single crystal size, cleanliness, and surface defects can all impact mobility measurements. Record single crystal mobility is reported by Chen et al.,[41] achieving a value of 43.9 cm^2 V^{-1} s^{-1} at a carrier concentration of 4.3 × 10^{16} cm^{-3} in a sample of dimensions 15 × 10 × 1 mm. This is in the

https://doi.org/10.1021/acs.chemmater.3c01628
Chem. Mater. 2023, 35, 8995−9006

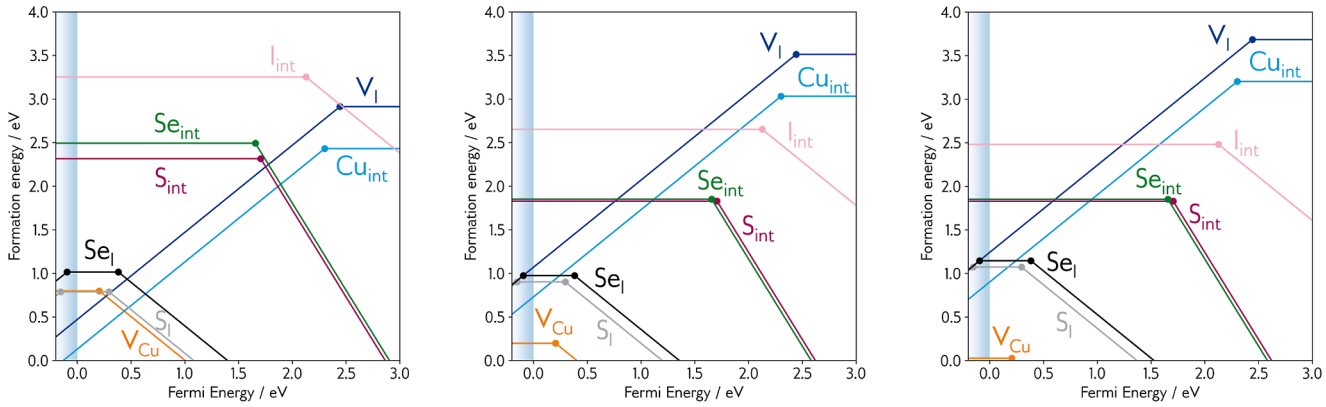

(a) Cu-rich, I-poor, chalcogen-poor. (b) Cu-mid, I-mid, chalcogen-rich. (c) Cu-poor, I-rich, chalcogen-rich.

Figure 6. Transition level diagrams for CuI under three sets of chemical potentials. Fermi energy (eV) on the *x*-axis, formation energy (eV) on *y*-axis. The valence band maximum (VBM) is denoted by the shaded blue region. The gradient of each line represents the charge state, and filled circles denote transition levels where two charge states are in thermodynamic equilibrium. (a) Cu-rich, I-poor, chalcogen-poor. (b) Cu-mid, I-mid, chalcogen-rich. (c) Cu-poor, I-rich, chalcogen-rich.

electron−phonon scattering limit and suggests significant scope for improvement in mobility at low carrier concentrations. Other single crystals have been synthesized by Lv et al.,[42] obtaining a sample of similar size and carrier concentration but with a reduced mobility of 12.8 $cm^2\ V^{-1}\ s^{-1}$, and Matsuzaki et al.,[97] achieving mobility up to 29 $cm^2\ V^{-1}\ s^{-1}$ at low concentrations ($2.0 \times 10^{14}\ cm^{-3}$) and 19 $cm^2\ V^{-1}\ s^{-1}$ at carrier concentrations approaching the degenerate conductivity limit. By considering the POP scattering rate from AMSET as the dominant low concentration scattering mechanism, Chen's measurement exceeds the predicted mobility. It is reasonable to assume that this single crystal measurement is within the "low" carrier concentration regime, as a rough calculation of the Mott criterion using the parabolic (transport) band edge effective masses and the experimental dielectric constant indicates a carrier density of 8.5×10^{17} cm^{-3} ($1.65 \times 10^{18}\ cm^{-3}$). This failure of the SERTA to describe the low carrier density experimental data points was the first indication that a more sophisticated treatment of the e−ph scattering would be required for CuI.

Turning now to thin films, the record mobility measurement is more difficult to identify. Several papers report promising mobilities, even surpassing the 43.9 $cm\ V^{-2}\ s^{-1}$ from Chen et al.: 35 $cm^2\ V^{-1}\ s^{-1}$ at $8.5 \times 10^{18}\ cm^{-3}$ via liquid iodization of metallic Cu from Wang et al.;[99] 35 to 50 $cm^2\ V^{-1}\ s^{-1}$ at concentrations in the region of $1 \times 10^{18}\ cm^{-3}$ via iodization of metallic Cu on crystalline Si substrates from Madkhali et al.;[100] and 110 $cm^2\ V^{-1}\ s^{-1}$ at $1.1 \times 10^{18}\ cm^{-3}$ via MBE on crystalline Si from Ahn et al.[101] However, these measurements are from extremely thin films that have XRD peaks that can be attributed to the Cu and c-Si substrates, which themselves are extremely good charge carriers, making it difficult to decouple the transport properties of the substrate from those of the film. These results are therefore omitted from Figure 5. Storm et al. report consistently high thin film mobility via pulsed laser deposition (PLD, purple triangles in Figure 5) over a wide range of carrier concentrations,[38,40] which comprises the most reliable thin film data available in the literature. At the higher end of the carrier concentrations reported, films deposited from sputtering and liquid iodization appear to approach the mobility limit arising from ionized impurity scattering, peaking around 10 $cm^2\ V^{-1}\ s^{-1}$. Across the entire carrier concentration range, the experimental results fall within the IBTE + IMP limit (and critically fall outside the SERTA + IMP, i.e., AMSET, limit), justifying our approach.

The final and perhaps most crucial point to consider is the electronic performance achievable via scalable synthesis methods. While PLD, MBE and sputtering offer reasonably high mobilities across the carrier concentration range, they are not commercially viable deposition techniques. Instead, inkjet printing, spin coating, and, potentially, iodination reactions are likely to be the most industrially relevant. The hole mobilities reported from these methods seldom exceed 10 $cm^2\ V^{-1}\ s^{-1}$ regardless of carrier concentration, owing to the lower crystallinity of the films and subsequent grain boundary and interface scattering. Such CuI films are roughly on par with SnO mobility,[15] but are beaten by Ba_2BiTaO_6 (30 $cm^2\ V^{-1}\ s^{-1}$)[19,20] and the layered oxychalcogenide $(Cu_2S_2)(Sr_3Sc_2O_5)$ (150 $cm^2\ V^{-1}\ s^{-1}$),[102] and are still up to 2 orders of magnitude lower than the degenerately doped n-type transparent conductors (In_2O_3 130 $cm^2\ V^{-1}\ s^{-1}$, Ga_2O_3 75 $cm^2\ V^{-1}\ s^{-1}$, SnO_2 130 $cm^2\ V^{-1}\ s^{-1}$, $BaSnO_3$ 320 $cm^2\ V^{-1}\ s^{-1}$, and $ZnSb_2O_6$ 49 $cm^2\ V^{-1}\ s^{-1}$).[103−107] Despite this, CuI has been successfully used to make thin film transistors via solution-based and inkjet deposition with competitive switching ratios and current densities,[37,43,108] and amorphous CuI thin-film transistors (TFTs) have been reported to outperform polycrystalline devices.[109] Such applications often require a carrier density lower than $10^{20}\ cm^{-3}$, where the mobility of CuI can be significantly improved. The prediction of such a large scope for improvement in CuI mobility indicates that other scattering processes may also be in play, such as surface and grain boundary scattering, which could be mitigated as deposition and device engineering process become more sophisticated. These results indicate that CuI will retain its position as the front-runner in the race for a marketable p-type TCM, and provide useful insights for quality control in CuI.

Defect Chemistry. Suitable point defect chemistry is crucial to the operation of transparent conducting materials. For a p-type system, it is necessary to have low formation

https://doi.org/10.1021/acs.chemmater.3c01628
Chem. Mater. 2023, 35, 8995−9006

energy acceptor defects at Fermi levels close to, or ideally within, the VBM. As the separation between the defect state and band edge decreases, more holes can be generated at the VBM through thermal excitation of an electron to the defect (with energy $\sim k_B T$), increasing conductivity. It is also desirable that such p-type defects generate delocalized charge density, enabling a high charge carrier mobility with no energetic barrier—the formation of localized charge, or hole polarons, necessitates an activation energy E_A (with an Arrhenius-like temperature dependency) for charge transport, which significantly reduces optoelectronic performance (consider the polaron-limited mobility in $CuAlO_2$ of 3 $cm^2\ V^{-1}\ s^{-1}$).[7,110] To this end, both the intrinsic defect chemistry of CuI and the effects of chalcogen doping (S and Se) were studied using hybrid functionals. Transition level diagrams under a variety of Cu−I chemical potentials (Cu-rich, midpoint, and Cu-poor) are shown in Figure 6, while tabulated formation energies of defects and competing phases, along with extended methodology, can be found in the Supporting Information.

Intrinsic Defects. The copper vacancy is the predominant defect in CuI, with a formation energy below 1 eV regardless of the growth conditions. It has a transition level from the 0/1— charge state approximately at 0.24 eV from the band edge, indicative of a deep defect. A significant disruption to the local crystal structure upon vacancy formation supports this behavior, with one nearby Cu atom relaxing toward the vacancy by 0.09 Å. The hole generated at the VBM by the formation of a copper vacancy is found to localize on this displaced atom, shown in Figure S6. However, analysis of the Fröhlich polaron constant for CuI (α = 0.44 for PBEsol and 1.55 for PBE0) indicates that such a polaron is likely to be spread over several unit cells (supported by observation of several metastable defect geometries within 1 meV of the ground state with less localized hole density, see Figures S5 and S6) so should still result in reasonable charge carrier mobility, and crucially indicates that the band carrier model assumed for the charge transport calculations is still valid. Under Cu-poor conditions, charge carrier concentrations of up to 2×10^{19} cm^{-3} are predicted solely due to the increased concentration of copper vacancies, indicating that this species is the key factor in controlling p-type conductivity in CuI.

The remaining intrinsic defect species are the p-type iodine interstitial (I_{int}), the n-type iodine vacancy (V_I), and the n-type copper interstitial (Cu_{int}). The iodine interstitial is an ultradeep acceptor with prohibitively high formation energies under all growth conditions (2.5 eV in the best case), and is unlikely to play a major role in boosting p-type conductivity. The n-type defects are both deep donors and under Cu-rich conditions are predicted to charge compensate the holes generated by the copper vacancy (where the blue and orange lines intersect in Figure 6a). However, as growth conditions are modulated toward a Cu-poor environment, the formation energies of both the iodine vacancy and copper interstitial are sufficiently raised such that they can no longer charge compensate.

Extrinsic Defects—Post Hoc Ergo Propter Hoc? Chalcogen (S, Se) doping has been explored as a route to further enhance hole conductivity both computationally and experimentally.[30,38,40,68] The formation energies of Cu_xS_y and Cu_xSe_y competing phases within the chemical potential limits of CuI control the chemical potentials of the dopant atoms, but it is observed that synthesis conditions have little effect on the formation energies of the substitutional species S_I and Se_I due to the concomitant changing chemical potential of iodine. Much larger changes in formation energy are observed for the interstitial defects S_{int} and Se_{int}, where the changing chemical potential of iodine has no impact on the formation energy of the chalcogen defect.

The substitutional defects themselves are higher in energy than the copper vacancy under p-type growth conditions (Figure 6b,c), at around 0.9 eV for S_I and 1.0 eV for Se_I, and have deeper transition levels. This suggests a greater degree of charge localization than for the copper vacancy, which is shown in Figure 7. The hole generated by the formation of

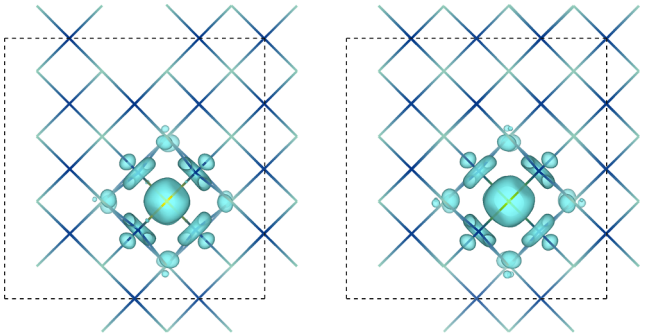

(a) S_I^0, 0.006 e Å^{-3}. (b) Se_I^0, 0.006 e Å^{-3}.

Figure 7. Partial hole density generated by various defects in CuI. Defect supercell is denoted by a dotted black line; blue regions are Cu, green regions are I, and lime green regions are dopants. (a) S_I^0, 0.006 e Å^{-3}. (b) Se_I^0, 0.006 e Å^{-3}.

both defects is strongly bound to the site of the substitution and causes a significant inward relaxation of the four surrounding copper atoms. This deep transition level is supported by the experimental work of Storm et al., who report a binding energy for the Se substitution of around 300 meV.[40] Graužinytė et al. predict shallower transition levels for both S_I and Se_I, but these are from defect relaxations performed with a semilocal exchange−correlation functional without SOC, leading to an overdelocalization of charge and an incorrect defect geometry.[68]

Finally, the interstitial chalcogen species are much higher in formation energy and are predicted to act as ultradeep acceptors, with negative-U 0/2—transitions occurring at Fermi levels close to 2.0 eV. These characteristics preclude them from having any significant effect on the electronic properties of CuI.

Overall, the defect chemistry of CuI is rather straightforward. Native p-type conductivity is enabled by the formation of copper vacancies, the concentration of which can be fine-tuned by strict control of the copper chemical potential during synthesis, while the remaining intrinsic species have little to no effect on the defect landscape. Despite the small improvements in electronic properties after doping with S and Se reported in the literature, these dopants are predicted to be electronically inactive with deep transition levels that result in significant charge trapping. This is an example of the logical fallacy post hoc, ergo propter hoc, or "after this, therefore because of this". A number of factors could contribute to the prediction of deeper transition levels in the current work compared to those from Graužinytė et al.: a more thorough exploration of the potential energy surface for each defect state via use of the ShakeNBreak method; full geometric optimization with hybrid functionals, rather than relaxation with semi-local functionals

https://doi.org/10.1021/acs.chemmater.3c01628
Chem. Mater. 2023, 35, 8995−9006

plus a hybrid functional single-shot on a volume-scaled structure; and the explicit inclusion of SOC during defect calculations to accurately model the position of the band edges. With these new insights on the electronic role of chalcogen dopants, it is instead proposed that indirect changes in host chemical potentials as a result of chalcogen doping have a greater impact on overall hole concentration. Furthermore, effects on crystallinity and morphology should be considered during experimental investigation of chalcogen doping, as this can be a further source of indirect improvements to optoelectronic performance.

CONCLUSIONS

This article examined the suitability of CuI as a high performance p-type transparent conductor. Using sophisticated charge transport modeling, an upper limit to hole mobility as a function of carrier concentration was predicted, ranging from 162 $cm^2 V^{-1} s^{-1}$ in the phonon-limited range to 32.6 $cm^2 V^{-1} s^{-1}$ in the degenerately doped, ionized impurity-limited range. These results suggest a significant scope for improvement in experimental mobility, particularly in the low to mid concentration range, which could be achieved by mitigating surface and grain boundary scattering processes and by further optimization of synthesis conditions. The prospect of achieving samples with mobilities that closely align with our theoretical projections holds significant promise. Such progress has the capacity to yield a noteworthy 2- to 3-fold enhancement in the existing experimental FoM, Φ, for CuI, thereby propelling it to a competitive stance alongside the finest n-type materials currently prevalent on the market. An examination of the defect chemistry revealed that the copper vacancy is the predominant source of charge carriers in CuI and that modulation of the copper chemical potential during synthesis is key to controlling the hole concentration. The chalcogens S and Se are predicted to be electronically inactive dopants but can result in increased conductivity and hole concentration via indirect effects such as improved sample crystallinity. Revisiting nondoped CuI and exercising greater control over the copper vacancy could lead to enhanced mobility at lower carrier concentrations, which would improve the performance of CuI in thin film electronics. This work will act as a useful benchmark to experimental studies on CuI and related p-type transparent conductors and indicates that there is still scope for enhanced optoelectronic performance.

ASSOCIATED CONTENT

Supporting Information

The Supporting Information is available free of charge at https://pubs.acs.org/doi/10.1021/acs.chemmater.3c01628.

Phonon dispersion, charge transport constants, further AMSET plots, and convergence testing (PDF)

AUTHOR INFORMATION

Corresponding Authors

Geoffroy Hautier − *UCLouvain, Institute of Condensed Matter and Nanosciences (IMCN), Louvain-la-Neuve B-1348, Belgium; Thayer School of Engineering, Dartmouth College, Hanover, New Hampshire 03755, United States*; Email: geoffroy.hautier@dartmouth.edu

David O. Scanlon − *Department of Chemistry, University College London, London WC1H 0AJ, U.K.; Thomas Young Centre, University College London, London WC1E 6BT, U.K.; School of Chemistry, University of Birmingham, Edgbaston, Birmingham B15 2TT, U.K.*; orcid.org/0000-0001-9174-8601; Email: d.o.scanlon@bham.ac.uk

Authors

Joe Willis − *Department of Chemistry, University College London, London WC1H 0AJ, U.K.; Thomas Young Centre, University College London, London WC1E 6BT, U.K.*; orcid.org/0000-0002-1900-2677

Romain Claes − *UCLouvain, Institute of Condensed Matter and Nanosciences (IMCN), Louvain-la-Neuve B-1348, Belgium*

Qi Zhou − *Department of Chemistry, University College London, London WC1H 0AJ, U.K.; Thomas Young Centre, University College London, London WC1E 6BT, U.K.*

Matteo Giantomassi − *UCLouvain, Institute of Condensed Matter and Nanosciences (IMCN), Louvain-la-Neuve B-1348, Belgium*

Gian-Marco Rignanese − *UCLouvain, Institute of Condensed Matter and Nanosciences (IMCN), Louvain-la-Neuve B-1348, Belgium*; orcid.org/0000-0002-1422-1205

Complete contact information is available at: https://pubs.acs.org/10.1021/acs.chemmater.3c01628

Author Contributions

#J.W. and R.C. contributed equally to this work.

Notes

The authors declare no competing financial interest.

Online repository which can be found at DOI: https://doi.org/10.5281/zenodo.8318329 contains charge transport and defect formation energy data.

ACKNOWLEDGMENTS

J.W. and R.C. acknowledge fruitful discussions with Dr Andrea Crovetto, Dr Alex Squires, Dr Alex Ganose, Dr Chris Savory, and Dr Guillaume Brunin. J.W. and D.O.S. acknowledge Diamond Light Source Ltd for cosponsorship of an EngD studentship on the EPSRC Centre for Doctoral Training in Molecular Modelling and Materials Science (EP/L015862/1), support for EPSRC Grant number EP/N01572X/1, and from the European Research Council, ERC (grant no. 758345). This work used the ARCHER and ARCHER2 UK National Supercomputing Service (https://www.archer2.ac.uk), via our membership of the UK's HEC Materials Chemistry Consortium, which is funded by EPSRC (EP/L000202, EP/R029431, and EP/T022213). We are grateful to the UK Materials and Molecular Modelling Hub for computational resources (Thomas and Young), which is partially funded by EPSRC (EP/P020194/1 and EP/T022213/1). The authors acknowledge the use of the UCL Myriad, Kathleen, and Thomas High Performance Computing Facilities (Myriad@UCL, Kathleen@UCL, and Thomas@UCL), and associated support services, in the completion of this work. R.C. acknowledges financial support from the Communauté Française de Belgique, grant ARC 18/23-093. G.M.R. acknowledges financial support from the Fonds de la Recherche Scientifique de Belgique (F.R.S.-FNRS). Computational resources were provided by the Consortium des Équipements de Calcul Intensif, funded by the F.R.S.- FNRS under grant no. 2.5020.11 and by the Walloon Region. The present research benefited from computational resources made available on the Tier-1 supercomputer of the Fédération

Wallonie-Bruxelles, infrastructure funded by the Walloon Region under grant no. 1117545. G.H. acknowledges funding by the U.S. Department of Energy, Office of Science, Office of Basic Energy Sciences, Materials Sciences and Engineering Division, under contract no. DE-AC02-05-CH11231: Materials Project program KC23MP. The work has received partial support from the European Union's Horizon 2020 research and innovation program, grant no. 951786 through the Center of Excellence NOMAD.

■ ADDITIONAL NOTE

[a]Generally, the figure of merit is calculated as the ratio between electrical conductivity σ and the visible absorption coefficient α, where T_{vis} is transmission and R_s is the sheet resistance, related to conductivity and thickness d.

■ REFERENCES

(1) Kawazoe, H.; Yasukawa, M.; Hyodo, H.; Kurita, M.; Yanagi, H.; Hosono, H. P-type electrical conduction in transparent thin films of $CuAlO_2$. *Nature* **1997**, *389*, 939−942.

(2) Scanlon, D. O.; Walsh, A.; Morgan, B. J.; Watson, G. W.; Payne, D. J.; Egdell, R. G. Effect of Cr substitution on the electronic structure of $CuAl_{(1-x)}Cr_{(x)}O_2$. *Phys. Rev. B* **2009**, *79*, 035101.

(3) Arnold, T.; Payne, D. J.; Bourlange, A.; Hu, J. P.; Egdell, R. G.; Piper, L. F. J.; Colakerol, L.; De Masi, A.; Glans, P. A.; Learmonth, T.; et al. X-ray spectroscopic study of the electronic structure of $CuCrO_2$. *Phys. Rev. B* **2009**, *79*, 075102.

(4) Shin, D.; Foord, J. S.; Payne, D. J.; Arnold, T.; Aston, D. J.; Egdell, R. G.; Godinho, K. G.; Scanlon, D. O.; Morgan, B. J.; Watson, G. W.; et al. Comparative study of bandwidths in copper delafossites from x-ray emission spectroscopy. *Phys. Rev. B* **2009**, *80*, 233105.

(5) Scanlon, D. O.; Morgan, B. J.; Watson, G. W.; Walsh, A. Acceptor Levels in p-type Cu_2O: Rationalizing Theory and Experiment. *Phys. Rev. Lett.* **2009**, *103*, 096405.

(6) Scanlon, D. O.; Walsh, A.; Watson, G. W. Understanding the p-Type Conduction Properties of the Transparent Conducting Oxide $CuBO_2$: A Density Functional Theory Analysis. *Chem. Mater.* **2009**, *21*, 4568−4576.

(7) Scanlon, D. O.; Watson, G. W. Conductivity Limits in $CuAlO_2$ from Screened-Hybrid Density Functional Theory. *J. Phys. Chem. Lett.* **2010**, *1*, 3195−3199.

(8) Scanlon, D. O.; Watson, G. W. Undoped n-type Cu_2O: Fact or Fiction? *J. Phys. Chem. Lett.* **2010**, *1*, 2582−2585.

(9) Scanlon, D. O.; Godinho, K. G.; Morgan, B. J.; Watson, G. W. Understanding conductivity anomalies in Cu(I)-based delafossite transparent conducting oxides: Theoretical insights. *J. Chem. Phys.* **2010**, *132*, 024707.

(10) Godinho, K. G.; Carey, J. J.; Morgan, B. J.; Scanlon, D. O.; Watson, G. W. Understanding conductivity in $SrCu_2O_2$: stability, geometry and electronic structure of intrinsic defects from first principles. *J. Mater. Chem.* **2010**, *20*, 1086−1096.

(11) Scanlon, D. O.; Watson, G. W. Understanding the p-type defect chemistry of $CuCrO_2$. *J. Mater. Chem.* **2011**, *21*, 3655.

(12) Godinho, K. G.; Morgan, B. J.; Allen, J. P.; Scanlon, D. O.; Watson, G. W. Chemical bonding in copper-based transparent conducting oxides: $CuMO_2$ (M = In, Ga, Sc). *J. Phys.: Condens. Matter* **2011**, *23*, 334201.

(13) Scanlon, D. O.; Buckeridge, J.; Catlow, C. R. A.; Watson, G. W. Understanding doping anomalies in degenerate p-type semiconductor LaCuOSe. *J. Mater. Chem. C* **2014**, *2*, 3429−3438.

(14) Zhang, J. Y.; Li, W. W.; Hoye, R. L. Z.; MacManus-Driscoll, J. L.; Budde, M.; Bierwagen, O.; Wang, L.; Du, Y.; Wahila, M. J.; Piper, L. F. J.; Lee, T.-L.; Edwards, H. J.; Dhanak, V. R.; Zhang, K. H. L. Electronic and transport properties of Li-doped NiO epitaxial thin films. *J. Mater. Chem. C* **2018**, *6*, 2275−2282.

(15) Quackenbush, N. F.; Allen, J. P.; Scanlon, D. O.; Sallis, S.; Hewlett, J. A.; Nandur, A. S.; Chen, B.; Smith, K. E.; Weiland, C.; Fischer, D. A.; Woicik, J. C.; White, B. E.; Watson, G. W.; Piper, L. F. J. Origin of the Bipolar Doping Behavior of SnO from X-ray Spectroscopy and Density Functional Theory. *Chem. Mater.* **2013**, *25*, 3114−3123.

(16) Li, Y.; Singh, D. J.; Du, M.-H.; Xu, Q.; Zhang, L.; Zheng, W.; Ma, Y. Design of ternary alkaline-earth metal Sn(II) oxides with potential good p-type conductivity. *J. Mater. Chem. C* **2016**, *4*, 4592−4599.

(17) Zhang, K. H. L.; Du, Y.; Papadogianni, A.; Bierwagen, O.; Sallis, S.; Piper, L. F. J.; Bowden, M. E.; Shutthanandan, V.; Sushko, P. V.; Chambers, S. A. Perovskite Sr-Doped $LaCrO_3$ as a New p-Type Transparent Conducting Oxide. *Adv. Mater.* **2015**, *27*, 5191−5195.

(18) Amini, M. N.; Dixit, H.; Saniz, R.; Lamoen, D.; Partoens, B. The origin of p-type conductivity in ZnM_2O_4 (M = Co, Rh, Ir) spinels. *Phys. Chem. Chem. Phys.* **2014**, *16*, 2588.

(19) Bhatia, A.; Hautier, G.; Nilgianskul, T.; Miglio, A.; Sun, J.; Kim, H. J.; Kim, K. H.; Chen, S.; Rignanese, G.-M.; Gonze, X.; Suntivich, J. High-Mobility Bismuth-based Transparent p-Type Oxide from High-Throughput Material Screening. *Chem. Mater.* **2016**, *28*, 30−34.

(20) Shi, J.; Rubinstein, E. A.; Li, W.; Zhang, J.; Yang, Y.; Lee, T.-L.; Qin, C.; Yan, P.; MacManus-Driscoll, J. L.; Scanlon, D. O.; Zhang, K. H. Modulation of the Bi^{3+} $6s^2$ Lone Pair State in Perovskites for High-Mobility p-Type Oxide Semiconductors. *Advanced Science* **2022**, *9*, 2104141.

(21) Williamson, B. A. D.; Buckeridge, J.; Brown, J.; Ansbro, S.; Palgrave, R. G.; Scanlon, D. O. Engineering Valence Band Dispersion for High Mobility p-Type Semiconductors. *Chem. Mater.* **2017**, *29*, 2402−2413.

(22) Varley, J. B.; Miglio, A.; Ha, V.-A.; van Setten, M. J.; Rignanese, G.-M.; Hautier, G. High-Throughput Design of Non-oxide p-Type Transparent Conducting Materials: Data Mining, Search Strategy, and Identification of Boron Phosphide. *Chem. Mater.* **2017**, *29*, 2568−2573.

(23) Williamson, B. A. D.; Limburn, G. J.; Watson, G. W.; Hyett, G.; Scanlon, D. O. Computationally Driven Discovery of Layered Quinary Oxychalcogenides: Potential p-Type Transparent Conductors? *Matter* **2020**, *3*, 759−781.

(24) Willis, J.; Scanlon, D. O. Latest directions in p-type transparent conductor design. *J. Mater. Chem. C* **2021**, *9*, 11995−12009.

(25) Willis, J.; Bravić, I.; Schnepf, R. R.; Heinselman, K. N.; Monserrat, B.; Unold, T.; Zakutayev, A.; Scanlon, D. O.; Crovetto, A. Prediction and realisation of high mobility and degenerate p-type conductivity in CaCuP thin films. *Chem. Sci.* **2022**, *13*, 5872−5883.

(26) Crovetto, A.; Adamczyk, J. M.; Schnepf, R. R.; Perkins, C. L.; Hempel, H.; Bauers, S. R.; Toberer, E. S.; Tamboli, A. C.; Unold, T.; Zakutayev, A. Boron Phosphide Films by Reactive Sputtering: Searching for a P-Type Transparent Conductor. *Adv. Mater. Interfaces* **2022**, *9*, 2200031.

(27) Bädeker, K. Über die elektrische Leitfähigkeit und die thermoelektrische Kraft einiger Schwermetallverbindungen. *Ann. Phys.* **1907**, *327*, 749−766.

(28) Grundmann, M.; Schein, F.-L.; Lorenz, M.; Böntgen, T.; Lenzner, J.; von Wenckstern, H. Cuprous iodide - a p-type transparent semiconductor: history and novel applications. *Phys. Status Solidi A* **2013**, *210*, 1671−1703.

(29) Yang, C.; Kneiß, M.; Lorenz, M.; Grundmann, M. Room-temperature synthesized copper iodide thin film as degenerate p-type transparent conductor with a boosted figure of merit. *Proc. Natl. Acad. Sci. U.S.A.* **2016**, *113*, 12929−12933.

(30) Ahn, K.; Kim, G. H.; Kim, S.-J.; Kim, J.; Ryu, G.-S.; Lee, P.; Ryu, B.; Cho, J. Y.; Kim, Y.-H.; Kang, J.; Kim, H.; Noh, Y.-Y.; Kim, M.-G. Highly Conductive p-Type Transparent Conducting Electrode with Sulfur-Doped Copper Iodide. *Chem. Mater.* **2022**, *34*, 10517−10527.

(31) Ferhat, M.; Zaoui, A.; Certier, M.; Dufour, J.; Khelifa, B. Electronic structure of the copper halides CuCl, CuBr and CuI. *Mater. Sci. Eng. B* **1996**, *39*, 95−100.

(32) Yu, H.; Cai, X.; Yang, Y.; Wang, Z.-H.; Wei, S.-H. Band gap anomaly in cuprous halides. *Comput. Mater. Sci.* **2022**, *203*, 111157.

(33) Crovetto, A.; Hempel, H.; Rusu, M.; Choubrac, L.; Kojda, D.; Habicht, K.; Unold, T. Water Adsorption Enhances Electrical Conductivity in Transparent P-Type CuI. *ACS Appl. Mater. Interfaces* **2020**, *12*, 48741−48747.
(34) Yamada, N.; Ino, R.; Ninomiya, Y. Truly Transparent p-Type CuI Thin Films with High Hole Mobility. *Chem. Mater.* **2016**, *28*, 4971−4981.
(35) Peng, W.; Li, L.; Yu, S.; Yang, P.; Xu, K.; Luo, W. High-performance flexible transparent p-CuI film by optimized solid iodization. *Vacuum* **2021**, *183*, 109862.
(36) Vora-ud, A.; Chaarmart, K.; Kasemsin, W.; Boonkirdram, S.; Seetawan, T. Transparent thermoelectric properties of copper iodide thin films. *Phys. B* **2022**, *625*, 413527.
(37) Choi, C.-H.; Gorecki, J. Y.; Fang, Z.; Allen, M.; Li, S.; Lin, L.-Y.; Cheng, C.-C.; Chang, C.-H. Low-temperature, inkjet printed p-type copper(I) iodide thin film transistors. *J. Mater. Chem. C* **2016**, *4*, 10309−10314.
(38) Storm, P.; Bar, M. S.; Benndorf, G.; Selle, S.; Yang, C.; von Wenckstern, H.; Grundmann, M.; Lorenz, M. High mobility, highly transparent, smooth, p-type CuI thin films grown by pulsed laser deposition. *APL Mater.* **2020**, *8*, 091115.
(39) Inagaki, S.; Nakamura, M.; Aizawa, N.; Peng, L. C.; Yu, X. Z.; Tokura, Y.; Kawasaki, M. Molecular beam epitaxy of high-quality CuI thin films on a low temperature grown buffer layer. *Appl. Phys. Lett.* **2020**, *116*, 192105.
(40) Storm, P.; Bar, M. S.; Selle, S.; von Wenckstern, H.; Grundmann, M.; Lorenz, M. p-Type Doping and Alloying of CuI Thin Films with Selenium. *Phys. Status Solidi RRL* **2021**, *15*, 2100214.
(41) Chen, D.; Wang, Y.; Lin, Z.; Huang, J.; Chen, X.; Pan, D.; Huang, F. Growth Strategy and Physical Properties of the High Mobility P-Type CuI Crystal. *Cryst. Growth Des.* **2010**, *10*, 2057−2060.
(42) Lv, Y.; Xu, Z.; Ye, L.; Zhang, Z.; Su, G.; Zhuang, X. Large CuI semiconductor single crystal growth by a temperature reduction method from an NH_4I aqueous solution. *CrystEngComm* **2015**, *17*, 862−867.
(43) Liu, A.; Zhu, H.; Park, W.-T.; Kim, S.-J.; Kim, H.; Kim, M.-G.; Noh, Y.-Y. High-performance p-channel transistors with transparent Zn doped-CuI. *Nat. Commun.* **2020**, *11*, 4309.
(44) He, T.; Zhou, Y.; Yuan, P.; Yin, J.; Gutiérrez-Arzaluz, L.; Chen, S.; Wang, J.-X.; Thomas, S.; Alshareef, H. N.; Bakr, O. M.; Mohammed, O. F. Copper Iodide Inks for High-Resolution X-ray Imaging Screens. *ACS Energy Lett.* **2023**, *8*, 1362−1370.
(45) Schein, F.-L.; von Wenckstern, H.; Grundmann, M. Transparent p-CuI/n-ZnO heterojunction diodes. *Appl. Phys. Lett.* **2013**, *102*, 092109.
(46) Annadi, A.; Zhang, N.; Boon Kiang Lim, D.; Gong, H. New Transparent Magnetic Semiconductor $Ni_xCu_{1-x}I$ which Can Perform as Either P-type or N-type and Success in the P−N Homojunction Diode. *ACS Appl. Mater. Interfaces* **2020**, *12*, 6048−6055.
(47) Lee, J. H.; Lee, W.-J.; Kim, T. H.; Lee, T.; Hong, S.; Kim, K. H. Transparent p-CuI/n-$BaSnO_3$- δ heterojunctions with a high rectification ratio. *J. Phys.: Condens. Matter* **2017**, *29*, 384004.
(48) Ding, K.; Hu, Q.; Chen, D.; Zheng, Q.; Xue, X.; Huang, F. Fabrication and energy band alignment of n-ZnO/p-CuI heterojunction. *IEEE Electron Device Lett.* **2012**, *33*, 1750−1752.
(49) Cha, J.-H.; Jung, D.-Y. Air-stable transparent silver iodide−copper iodide heterojunction diode. *ACS Appl. Mater. Interfaces* **2017**, *9*, 43807−43813.
(50) Yang, C.; Kneiß, M.; Schein, F.-L.; Lorenz, M.; Grundmann, M. Room-temperature domain-epitaxy of copper iodide thin films for transparent CuI/ZnO heterojunctions with high rectification ratios larger than 109. *Sci. Rep.* **2016**, *6*, 21937.
(51) Liu, A.; Zhu, H.; Kim, M.-G.; Kim, J.; Noh, Y.-Y. Engineering copper iodide (CuI) for multifunctional p-type transparent semiconductors and conductors. *Advanced Science* **2021**, *8*, 2100546.
(52) Kresse, G.; Hafner, J. Ab initio molecular dynamics for liquid metals. *Phys. Rev. B* **1993**, *47*, 558−561.
(53) Kresse, G.; Hafner, J. Ab initio molecular-dynamics simulation of the liquid-metal−amorphous-semiconductor transition in germanium. *Phys. Rev. B* **1994**, *49*, 14251−14269.
(54) Blöchl, P. E. Projector augmented-wave method. *Phys. Rev. B* **1994**, *50*, 17953−17979.
(55) Kresse, G.; Hafner, J. Norm-conserving and ultrasoft pseudopotentials for first-row and transition elements. *J. Phys.: Condens. Matter* **1994**, *6*, 8245−8257.
(56) Kresse, G.; Furthmüller, J. Efficiency of ab-initio total energy calculations for metals and semiconductors using a plane-wave basis set. *Comput. Mater. Sci.* **1996**, *6*, 15−50.
(57) Kresse, G.; Furthmüller, J. Efficient iterative schemes for ab inition total-energy calculations using a plane-wave basis set. *Phys. Rev. B* **1996**, *54*, 11169−11186.
(58) Kresse, G.; Joubert, D. From ultrasoft pseudopotentials to the projector augmented-wave method. *Phys. Rev. B* **1999**, *59*, 1758−1775.
(59) Perdew, J. P.; Ruzsinszky, A.; Csonka, G. I.; Vydrov, O. A.; Scuseria, G. E.; Constantin, L. A.; Zhou, X.; Burke, K. Restoring the Density-Gradient Expansion for Exchange in Solids and Surfaces. *Phys. Rev. Lett.* **2008**, *100*, 136406.
(60) Perdew, J. P.; Ernzerhof, M.; Burke, K. Rationale for mixing exact exchange with density functional approximations. *J. Chem. Phys.* **1996**, *105*, 9982−9985.
(61) Gonze, X.; Amadon, B.; Antonius, G.; Arnardi, F.; Baguet, L.; Beuken, J.-M.; Bieder, J.; Bottin, F.; Bouchet, J.; Bousquet, E.; et al. The ABINIT project: Impact, environment and recent developments. *Comput. Phys. Commun.* **2020**, *248*, 107042.
(62) Romero, A. H.; Allan, D. C.; Amadon, B.; Antonius, G.; Applencourt, T.; Baguet, L.; Bieder, J.; Bottin, F.; Bouchet, J.; Bousquet, E.; et al. ABINIT: Overview and focus on selected capabilities. *J. Chem. Phys.* **2020**, *152*, 124102.
(63) Brunin, G.; Miranda, H. P. C.; Giantomassi, M.; Royo, M.; Stengel, M.; Verstraete, M. J.; Gonze, X.; Rignanese, G.-M.; Hautier, G. Electron-phonon beyond Fröhlich: dynamical quadrupoles in polar and covalent solids. *Phys. Rev. Lett.* **2020**, *125*, 136601.
(64) Brunin, G.; Miranda, H. P. C.; Giantomassi, M.; Royo, M.; Stengel, M.; Verstraete, M. J.; Gonze, X.; Rignanese, G.-M.; Hautier, G. Phonon-limited electron mobility in Si, GaAs, and GaP with exact treatment of dynamical quadrupoles. *Phys. Rev. B* **2020**, *102*, 094308.
(65) Claes, R.; Brunin, G.; Giantomassi, M.; Rignanese, G.-M.; Hautier, G. Assessing the quality of relaxation-time approximations with fully automated computations of phonon-limited mobilities. *Phys. Rev. B* **2022**, *106*, 094302.
(66) M Ganose, A.; J Jackson, A.; O Scanlon, D. sumo: Command-line tools for plotting and analysis of periodic ab initio calculations. *J. Open Source Softw.* **2018**, *3*, 717.
(67) Petretto, G.; Dwaraknath, S.; Miranda, H. P.; Winston, D.; Giantomassi, M.; Van Setten, M. J.; Gonze, X.; Persson, K. A.; Hautier, G.; Rignanese, G.-M. High-throughput density-functional perturbation theory phonons for inorganic materials. *Sci. Data* **2018**, *5*, 180065.
(68) Graužinytė, M.; Botti, S.; Marques, M. A. L.; Goedecker, S.; Flores-Livas, J. A. Computational acceleration of prospective dopant discovery in cuprous iodide. *Phys. Chem. Chem. Phys.* **2019**, *21*, 18839−18849.
(69) Mosquera-Lois, I.; Kavanagh, S. R.; Walsh, A.; Scanlon, D. O. ShakeNBreak: Navigating the defect configurational landscape. *J. Open Source Softw.* **2022**, *7*, 4817.
(70) Mosquera-Lois, I.; Kavanagh, S. R.; Walsh, A.; Scanlon, D. O. Identifying the ground state structures of point defects in solids. *npj Comput. Mater.* **2023**, *9*, 25.
(71) Persson, C.; Zhao, Y.-J.; Lany, S.; Zunger, A. n-type doping of $CuInSe_2$ and $CuGaSe_2$. *Phys. Rev. B* **2005**, *72*, 035211.
(72) Lany, S.; Zunger, A. Assessment of correction methods for the band-gap problem and for finite-size effects in supercell defect calculations: Case studies for ZnO and GaAs. *Phys. Rev. B* **2008**, *78*, 235104.

https://doi.org/10.1021/acs.chemmater.3c01628
Chem. Mater. 2023, 35, 8995−9006

(73) Lany, S.; Zunger, A. Accurate prediction of defect properties in density functional supercell calculations. *Modell. Simul. Mater. Sci. Eng.* **2009**, *17*, 084002.
(74) Murphy, S. T.; Hine, N. D. M. Anisotropic charge screening and supercell size convergence of defect formation energies. *Phys. Rev. B* **2013**, *87*, 094111.
(75) Buckeridge, J. Equilibrium point defect and charge carrier concentrations in a material determined through calculation of the self-consistent Fermi energy. *Comput. Phys. Commun.* **2019**, *244*, 329−342.
(76) Squires, A. G.; Scanlon, D. O.; Morgan, B. J. py-sc-fermi: self-consistent Fermi energies and defect concentrations from electronic structure calculations. *J. Open Source Softw.* **2023**, *8*, 4962.
(77) D Whalley, L. effmass: An effective mass package. *J. Open Source Softw.* **2018**, *3*, 797.
(78) Whalley, L. D.; Frost, J. M.; Morgan, B. J.; Walsh, A. Impact of nonparabolic electronic band structure on the optical and transport properties of photovoltaic materials. *Phys. Rev. B* **2019**, *99*, 085207.
(79) Keen, D. A.; Hull, S. The high-temperature structural behaviour of copper(I) iodide. *J. Phys.: Condens. Matter* **1995**, *7*, 5793−5804.
(80) Moditswe, C.; Muiva, C. M.; Luhanga, P.; Juma, A. Effect of annealing temperature on structural and optoelectronic properties of CuI thin films prepared by the thermal evaporation method. *Ceram. Int.* **2017**, *43*, 5121−5126.
(81) Ves, S.; Glötzel, D.; Cardona, M.; Overhof, H. Pressure dependence of the optical properties and the band structure of the copper and silver halides. *Phys. Rev. B* **1981**, *24*, 3073−3085.
(82) Blacha, A.; Cardona, M.; Christensen, N.; Ves, S.; Overhof, H. Volume dependence of the spin-orbit splitting in the copper halides. *Physica B+C* **1983**, *117−118*, 63−65.
(83) Ganose, A. M.; Park, J.; Faghaninia, A.; Woods-Robinson, R.; Persson, K. A.; Jain, A. Efficient calculation of carrier scattering rates from first principles. *Nat. Commun.* **2021**, *12*, 2222.
(84) Hennion, B.; Moussa, F.; Prevot, B.; Carabatos, C.; Schawb, C. Normal Modes of Vibrations in CuI. *Phys. Rev. Lett.* **1972**, *28*, 964−966.
(85) Fukumoto, T.; Nakashima, S.; Tabuchi, K.; Mitsuishi, A. Temperature Dependence of Raman Spectra of Cuprous Halides. *Phys. Status Solidi B* **1976**, *73*, 341−351.
(86) Hanson, R.; Hallberg, J.; Schwab, C. Elastic and piezoelectric constants of the cuprous halides. *Appl. Phys. Lett.* **1972**, *21*, 490−492.
(87) Skelton, J. M.; Gunn, D. S. D.; Metz, S.; Parker, S. C. Accuracy of Hybrid Functionals with Non-Self-Consistent Kohn−Sham Orbitals for Predicting the Properties of Semiconductors. *J. Chem. Theory Comput.* **2020**, *16*, 3543−3557.
(88) Onida, G.; Reining, L.; Rubio, A. Electronic excitations: density-functional versus many-body Green's-function approaches. *Rev. Mod. Phys.* **2002**, *74*, 601−659.
(89) Li, Y.; Sun, J.; Singh, D. J. Optical and electronic properties of doped p -type CuI: Explanation of transparent conductivity from first principles. *Phys. Rev. Mater.* **2018**, *2*, 035003.
(90) Poncé, S.; Margine, E. R.; Giustino, F. Towards predictive many-body calculations of phonon-limited carrier mobilities in semiconductors. *Phys. Rev. B* **2018**, *97*, 121201.
(91) Meng, F.; Ma, J.; He, J.; Li, W. Phonon-limited carrier mobility and temperature-dependent scattering mechanism of 3C-SiC from first principles. *Phys. Rev. B* **2019**, *99*, 045201.
(92) Ma, J.; Nissimagoudar, A. S.; Li, W. First-principles study of electron and hole mobilities of Si and GaAs. *Phys. Rev. B* **2018**, *97*, 045201.
(93) Prasad, M.; Gupta, S. Hall effect measurement of a $CuI_{1.0046}$ pellet. *Phys. Status Solidi A* **1986**, *94*, K65−K68.
(94) Knauth, P.; Massiani, Y.; Pasquinelli, M. Semiconductor properties of polycrystalline CuBr by Hall effect and capacitive measurements. *Phys. Status Solidi A* **1998**, *165*, 461−465.
(95) Yang, C.; Souchay, D.; Kneiß, M.; Bogner, M.; Wei, H. M.; Lorenz, M.; Oeckler, O.; Benstetter, G.; Fu, Y. Q.; Grundmann, M. Transparent flexible thermoelectric material based on non-toxic earth-abundant p-type copper iodide thin film. *Nat. Commun.* **2017**, *8*, 16076.
(96) Li, Z. H.; He, J. X.; Lv, X. H.; Chi, L. F.; Egbo, K. O.; Li, M.-D.; Tanaka, T.; Guo, Q. X.; Yu, K. M.; Liu, C. P. Optoelectronic properties and ultrafast carrier dynamics of copper iodide thin films. *Nat. Commun.* **2022**, *13*, 6346.
(97) Matsuzaki, K.; Tsunoda, N.; Kumagai, Y.; Tang, Y.; Nomura, K.; Oba, F.; Hosono, H. Hole-Doping to a Cu(I)-Based Semiconductor with an Isovalent Cation: Utilizing a Complex Defect as a Shallow Acceptor. *J. Am. Chem. Soc.* **2022**, *144*, 16572−16578.
(98) Almasoudi, M.; Saeed, A.; Salah, N.; Alshahrie, A.; Hasan, P. M. Z.; Melaibari, A.; Koumoto, K. CuI. CuI: A Promising Halide for Thermoelectric Applications below 373 K. *ACS Appl. Energy Mater.* **2022**, *5*, 10177−10186.
(99) Wang, M.; Wei, H.; Wu, Y.; Yang, C.; Han, P.; Juan, F.; Chen, Y.; Xu, F.; Cao, B. Highly transparent and conductive γ-CuI films grown by simply dipping copper films into iodine solution. *Phys. B* **2019**, *573*, 45−48.
(100) Madkhali, O.; Jullien, M.; Giba, A. E.; Ghanbaja, J.; Mathieu, S.; Gendarme, C.; Migot, S.; Alajlani, Y.; Can, N.; Alnjiman, F.; Horwat, D.; Redjaimia, A.; Pierson, J. Blue emission and twin structure of p-type copper iodide thin films. *Surf. Interfaces* **2021**, *27*, 101500.
(101) Ahn, D.; Song, J. D.; Kang, S. S.; Lim, J. Y.; Yang, S. H.; Ko, S.; Park, S. H.; Park, S. J.; Kim, D. S.; Chang, H. J.; Chang, J. Intrinsically p-type cuprous iodide semiconductor for hybrid light-emitting diodes. *Sci. Rep.* **2020**, *10*, 3995.
(102) Liu, M.-L.; Wu, L.-B.; Huang, F.-Q.; Chen, L.-D.; Chen, I.-W. A promising p-type transparent conducting material: Layered oxysulfide $[Cu_2S_2]$ $[Sr_3Sc_2O_5]$. *J. Appl. Phys.* **2007**, *102*, 116108.
(103) Swallow, J. E. N.; Williamson, B. A. D.; Sathasivam, S.; Birkett, M.; Featherstone, T. J.; Murgatroyd, P. A. E.; Edwards, H. J.; Lebens-Higgins, Z. W.; Duncan, D. A.; Farnworth, M.; et al. Resonant doping for high mobility transparent conductors: the case of Mo-doped In_2O_3. *Mater. Horiz.* **2020**, *7*, 236−243.
(104) Zhang, J.; Willis, J.; Yang, Z.; Lian, X.; Chen, W.; Wang, L.-S.; Xu, X.; Lee, T.-L.; Chen, L.; Scanlon, D. O.; Zhang, K. H. Deep UV transparent conductive oxide thin films realized through degenerately doped wide-bandgap gallium oxide. *Cell Rep. Phys. Sci.* **2022**, *3*, 100801.
(105) Fukumoto, M.; Nakao, S.; Shigematsu, K.; Ogawa, D.; Morikawa, K.; Hirose, Y.; Hasegawa, T. High mobility approaching the intrinsic limit in Ta-doped SnO_2 films epitaxially grown on TiO_2 (001) substrates. *Sci. Rep.* **2020**, *10*, 6844.
(106) Kim, H. J.; Kim, U.; Kim, H. M.; Kim, T. H.; Mun, H. S.; Jeon, B.-G.; Hong, K. T.; Lee, W.-J.; Ju, C.; Kim, K. H.; Char, K. High Mobility in a Stable Transparent Perovskite Oxide. *Appl. Phys. Express* **2012**, *5*, 061102.
(107) Jackson, A. J.; Parrett, B. J.; Willis, J.; Ganose, A. M.; Leung, W. W. W.; Liu, Y.; Williamson, B. A. D.; Kim, T. K.; Hoesch, M.; Veiga, L. S. I.; et al. Computational Prediction and Experimental Realization of Earth-Abundant Transparent Conducting Oxide Ga-Doped $ZnSb_2O_6$. *ACS Energy Lett.* **2022**, *7*, 3807−3816.
(108) Lee, H.-A.; Yatsu, K.; Kim, T. I.; Kwon, H.-I.; Park, I.-J. Synthesis of Vacancy-Controlled Copper Iodide Semiconductor for High-Performance p-Type Thin-Film Transistors. *ACS Appl. Mater. Interfaces* **2022**, *14*, 56416−56426.
(109) Lee, H. J.; Lee, S.; Lee, K. H.; Hong, K. Amorphous copper iodide: a p-type semiconductor for solution processed p-channel thin-film transistors and inverters. *J. Mater. Chem. C* **2022**, *10*, 7815−7821.
(110) Tate, J.; Ju, H. L.; Moon, J. C.; Zakutayev, A.; Richard, A. P.; Russell, J.; McIntyre, D. H. Origin of p-type conduction in single-crystal $CuAlO_2$. *Phys. Rev. B* **2009**, *80*, 165206.

https://doi.org/10.1021/acs.chemmater.3c01628
Chem. Mater. 2023, 35, 8995−9006